

Topological Defects in Hexagonal Manganites: Inner Structure and Emergent Electrostatics

Megan E. Holtz,[†] Konstantin Shapovalov,^{‡,§} Julia A. Mundy,^{†,§} Celesta S. Chang,^{||} Zewu Yan,^{⊥,#} Edith Bourret,[#] David A. Muller,^{†,∇} Dennis Meier,^{*,||} and Andrés Cano^{*,‡}

[†]School of Applied and Engineering Physics, ^{||}Department of Physics, Cornell University, Ithaca, New York 14853, United States

[‡]CNRS, Université de Bordeaux, ICMCB, UPR 9048, 33600 Pessac, France

[§]Department of Material Science and Engineering, University of California, Berkeley, Berkeley, California 94720, United States

[⊥]Department of Physics, ETH Zürich, CH-8093 Zurich, Switzerland

[#]Materials Sciences Division, Lawrence Berkeley National Laboratory, Berkeley, California 94720, United States

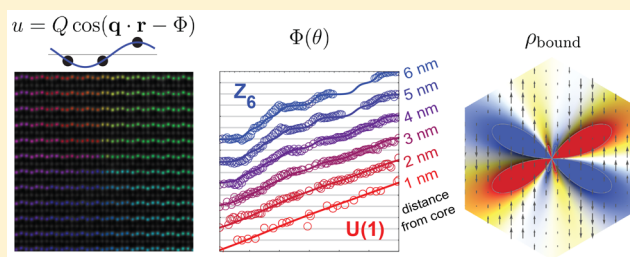
[∇]Kavli Institute at Cornell for Nanoscale Science, Ithaca, New York 14853, United States

^{*}Department of Materials Science and Engineering, Norwegian University of Science and Technology, 7491 Trondheim, Norway

S Supporting Information

ABSTRACT: Diverse topological defects arise in hexagonal manganites, such as ferroelectric vortices, as well as neutral and charged domain walls. The topological defects are intriguing because their low symmetry enables unusual couplings between structural, charge, and spin degrees of freedom, holding great potential for novel types of functional 2D and 1D systems. Despite the considerable advances in analyzing the different topological defects in hexagonal manganites, the understanding of their key intrinsic properties is still rather limited and disconnected. In particular, a rapidly increasing number of structural variants is reported without clarifying their relation, leading to a zoo of seemingly unrelated topological textures. Here, we combine picometer-precise scanning-transmission-electron microscopy with Landau theory modeling to clarify the inner structure of topological defects in $\text{Er}_{1-x}\text{Zr}_x\text{MnO}_3$. By performing a comprehensive parametrization of the inner atomic defect structure, we demonstrate that one primary length scale drives the morphology of both vortices and domain walls. Our findings lead to a unifying general picture of this type of structural topological defects. We further derive novel fundamental and universal properties, such as unusual bound-charge distributions and electrostatics at the ferroelectric vortex cores with emergent $U(1)$ symmetry.

KEYWORDS: Ferroics, topological defects, domain walls, ferroelectric vortices



Condensed-matter systems host a wide variety of topological defects that promote novel states of matter and unconventional phase transformations, such as the Kosterlitz–Thouless transition.^{1,2} Particularly interesting are the defects that arise in ferroic materials, with intriguing examples such as (multi)ferroic domain walls,³ discrete vortices,^{4,5} and skyrmions.⁶ These topologically protected nanotextures hold great potential for future device applications, for example, serving as information carriers in next-generation memory.^{7,8} Furthermore, they enable the study of universal, topology-driven phenomena related to otherwise inaccessible defects in the same universality class. This is exemplified in the current research trend to employ hexagonal manganites (RMnO_3 , $R = \text{Sc}, \text{Y}, \text{In}, \text{Dy}–\text{Lu}$) as test systems for cosmology related questions.^{9–11}

Recent high-resolution scanning probe measurements revealed an additional degree of complexity emerging from the structural topological defects in RMnO_3 .^{4,12–17} The

ferroelectric domain walls and vortices were found to exhibit very diverse—and seemingly unrelated—inner structures and properties.¹⁸ Pioneering domain wall studies on TmMnO_3 and YMnO_3 ,^{14,15} for instance, suggested the existence of atomically sharp and well-defined zigzag walls, whereas rather meandering and broadened walls were reported in ErMnO_3 and $\text{In}(\text{Mn,Ga})\text{O}_3$, respectively.^{19,20} Thus, in spite of the significant technical progress that has been made in imaging these atomic-scale objects, many findings remain intriguing but disconnected bits of information. Similarly, localized and spatially extended vortex structures were observed, with the identification of $U(1)$ symmetry emerging at the core of these vortices in $(\text{Y,In})\text{MnO}_3$ being a major new discovery.^{16,17} The zoo of experimental observations is mirrored by individual theoretical break-

Received: March 27, 2017

Revised: August 25, 2017

Published: September 5, 2017

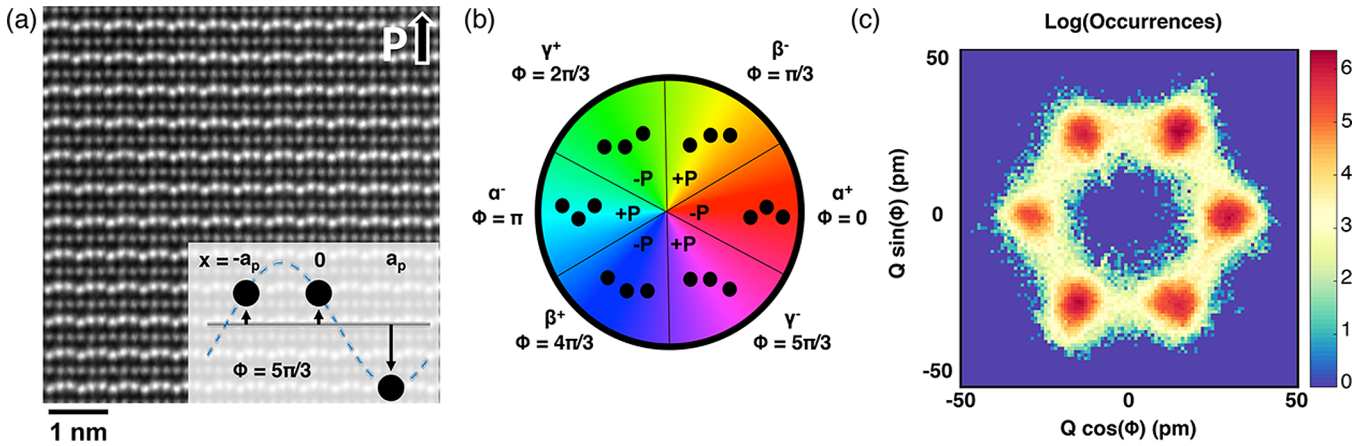


Figure 1. Ferroelectric displacement pattern and domain population. (a) High-angle annular dark field scanning transmission electron microscopy (HAADF-STEM) image of ErMnO_3 , viewed along the $P6_3cm$ $[1\bar{1}0]$ zone axis. The brighter Er atomic positions show the ferroelectric trimer distortion according to eq 1. (b) Sketch of the six possible structural domains with color overlay according to the phase Φ . (c) Histogram of the measured values of Q and Φ across 80 images near domain walls and three images with vortices, with the intensity on a logarithmic scale.

throughs applying notions as distant as homotopy groups and density functional theory (DFT).^{17,18,21,22}

In this work, we develop a unifying understanding of the inner structure of both structural domain walls and vortices in RMnO_3 . Combining high-angle annular dark field scanning transmission electron microscopy (HAADF-STEM) and Landau theory, we quantify the domain walls and vortices in the prototype improper ferroelectric ErMnO_3 . This quantification can be readily matched with previous descriptions based on density functional theory, and thus linked to the microscopic physics of these unconventional ferroelectrics.^{21–24}

Our findings reveal that, fundamentally, the inner structure of both domain walls and vortices is controlled by the same length scale (ξ_6).²⁵ In particular, we demonstrate the direct link between this length-scale and the emergence of $U(1)$ symmetry at the structural vortices. In addition, we find that this emergent $U(1)$ symmetry leads to unusual multipolar electrostatics, regardless of the properties of the surrounding domains.

Order Parameter and Domain States. The hexagonal manganite ErMnO_3 displays improper ferroelectricity ($T_c \approx 1470 \text{ K}$)²⁶ with a spontaneous polarization ($P||c$) of $\approx 6 \mu\text{C cm}^{-2}$ at room temperature.²⁵ This polarization emerges as a byproduct of the $P6_3/mmc$ symmetry breaking and the corresponding structural distortion.²³ The distortion follows the zone-boundary K_3 mode with wavevector $\mathbf{q} = (1/3, 1/3, 0)$ (in units of the lattice constant in the reciprocal space) and results in periodic tilts of the MnO_5 bipyramids and displacements of the Er ions along the c axis that triple the crystallographic unit cell. The overall distortion is such that the Er displacements display either an $\uparrow\downarrow\uparrow$ pattern, with positive polarization, or $\downarrow\downarrow\uparrow$ pattern with negative polarization.²⁷ Both positive and negative polarization patterns have three possible permutations, leading to a total of six structural domains.^{4,14–17,19,28,29}

Figure 1a shows a representative HAADF-STEM scan viewed down the $[1\bar{1}0]$ direction in ErMnO_3 [see Supporting Information (SI) Note 1 for details on acquisition and processing of STEM scans]. This image represents a single $\uparrow\downarrow\uparrow$ pattern of Er atoms as illustrated in the inset to Figure 1a. The Er displacements from the $P6_3/mmc$ paraelectric phase can be described by

$$u(\mathbf{r}_n) = u_0 + Q_1 \cos \mathbf{q} \cdot \mathbf{r}_n + Q_2 \sin \mathbf{q} \cdot \mathbf{r}_n \quad (1)$$

Here $u_0 \propto P$ represents a uniform distortion that can be related to the polar Γ_2^- mode, while $\mathbf{Q} = (Q_1, Q_2) \equiv (Q \cos \Phi, Q \sin \Phi)$ is the primary order parameter of the structural trimerization associated with the K_3 mode (the aforementioned tilt of the MnO_5 bipyramids can be parametrized by \mathbf{Q} in the same way, modulo a prefactor). The value Q represents the amplitude of the sinusoidal wave that describes the trimer distortion and relates the maximum displacement between erbium atoms to it as $1.5 \times Q$. Thus, eq 1 establishes the link between the observable atomic displacements and the key variable \mathbf{Q} of the trimerization transition (see also ref 16).

The transition into the trimerized state and the corresponding emergence of topological defects can be rationalized in terms of Landau theory,^{21,23,29} considering the free-energy expansion in powers of Q , Φ , and their gradients:

$$F(\mathbf{Q}; T) = \frac{a(T)}{2} Q^2 + \frac{b}{4} Q^4 + \frac{1}{6} (c + c' \cos^2 3\Phi) Q^6 + \frac{g}{2} [(\nabla Q)^2 + Q^2 (\nabla \Phi)^2] \quad (2)$$

This expansion represents the canonical Landau free energy in its simplest form, in which secondary variables are implicitly integrated out (so that P is automatically linked to \mathbf{Q} via the relation $P \sim Q^3 \cos 3\Phi$). As customary, the key dependence on the temperature is assumed to be $a(T) = a'(T - T_c)$. The parameters a' , b , c , and g represent positive constants. The coefficient c' , in contrast, determines whether the system develops a ferroelectric ($c' < 0$) or nonferroelectric ($c' > 0$) state according to the minimization of eq 2 and the P - Q relation.²⁹ Since ErMnO_3 is ferroelectric, we assume $c' < 0$ in the following.

The free energy (eq 2) contains two characteristic length scales. On one hand, we have the standard correlation length $\xi = \sqrt{g/|a(T)|}$ associated with the amplitude of the trimerization. On the other hand, we have the characteristic length $\xi_6 = \sqrt{g/(3c'|Q_0^4)} \simeq \xi \sqrt{b^2/(3|a(T)||c'|)}$ emerging below T_c in relation to the phase of the trimerization ($Q_0 \simeq \sqrt{|a(T)|/b}$ is the bulk value of the trimerization amplitude). These two length scales are a generic feature of the hexagonal manganites and their universality class.^{25,29} We

note that ξ_6 can be tuned by means of both temperature and chemical doping. Dopings of $\text{Er} \rightarrow \text{In}$ and $\text{Mn} \rightarrow \text{Ga}$, for instance, are expected to increase ξ_6 as they effectively reduce the Z_6 anisotropy ($\text{In}(\text{Ga},\text{Mn})\text{O}_3$ is nonferroelectric with $c' > 0^{20}$ and, hence, $lc' \rightarrow 0$ is expected during such dopings).

The Z_6 anisotropy term in eq 2 leads to the six symmetry-allowed trimerization domains illustrated in Figure 1b, which correspond to $\Phi_n = \frac{n\pi}{3}$ ($n = 0, 1, \dots, 5$) for $c' < 0$. Figure 1c shows the statistical analysis of \mathbf{Q} according to eq 1 obtained from multiple HAADF-STEM images covering $1.2 \times 10^4 \text{ nm}^2$. Six maxima are visible in the measured distribution of occurrences of Q and Φ , revealing that all six domain states are populated in our images of the ErMnO_3 sample.

Interestingly, Figure 1c also shows a finite population of trimerization states with $\Phi \neq \frac{n\pi}{3}$ other than the six discrete values found in bulk domains. This points toward additional trimerization features and a complex order-parameter distribution, which will be discussed in the following.

Charged and Neutral Domain Walls. We begin our analysis with isolated topological defects that arise in the form of ferroelectric domain walls. Figure 2a,b shows ErMnO_3

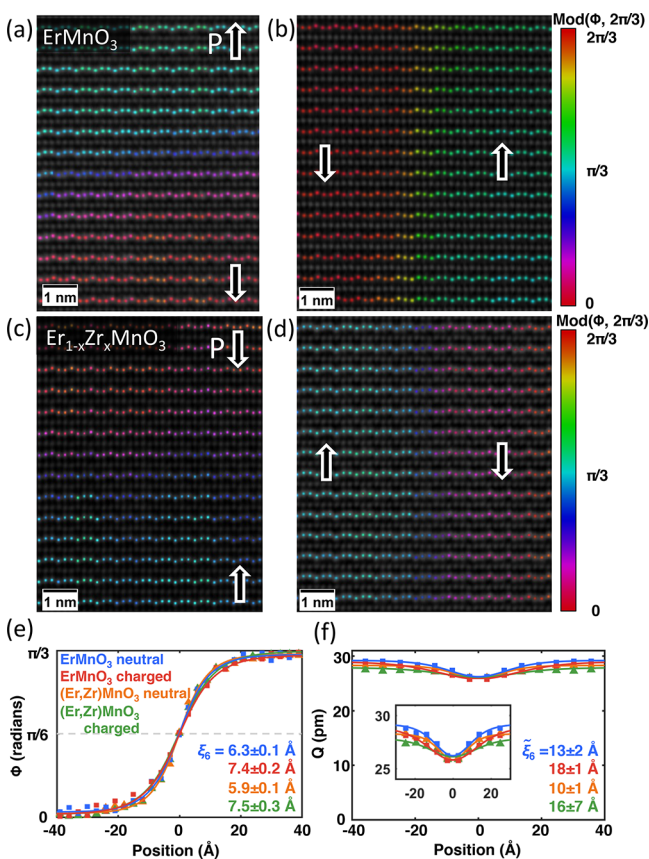


Figure 2. Inner structure of charged and neutral domain walls. (a–d) HAADF-STEM images of domain walls in ErMnO_3 (a,b) and $\text{Er}_{1-x}\text{Zr}_x\text{MnO}_3$, $x = 0.01$ (c,d) with color overlay of the phase according to eq 1. The following types of domain walls are identified: negatively charged tail-to-tail (a), positively charged head-to-head (c), and neutral (b,d) domain walls. (e,f) Quantification of the phase and the amplitude as a function of position relative to the domain wall center. Data are averaged across many neutral and charged domain walls in ErMnO_3 and $\text{Er}_{1-x}\text{Zr}_x\text{MnO}_3$, with ξ_6 and $\bar{\xi}_6$ measured by fitting to eqs 4 and 5.

HAADF-STEM images, where the displacement pattern of Er atoms changes gradually from positive to negative polarization: $\uparrow\uparrow\downarrow$ ($+P$) to $\downarrow\downarrow\uparrow$ ($-P$) up to a permutation. This inversion of the polarization (black arrows) implies the presence of ferroelectric 180° domain walls. Similar changes have been reported in other hexagonal manganites, demonstrating the general character of our observations (see, e.g., refs 14, 16, 17, and 20). Figure 2b shows a neutral domain wall, corresponding to the standard situation in proper ferroelectrics. Here the polarization is parallel to the wall, so that $\nabla \cdot \mathbf{P} = 0$. Thus, this wall avoids the emergence of bound charges. In Figure 2a we observe a different situation in which the change in \mathbf{P} is transverse to the wall ($\nabla \cdot \mathbf{P} \neq 0$). The latter represents a stable charged domain wall, which is a distinct fingerprint of the *improper* nature of the ferroelectricity in hexagonal manganites.¹²

To test the influence of perturbations in the electronic structure, we perform analogous measurements on $\text{Er}_{1-x}\text{Zr}_x\text{MnO}_3$ ($x = 0.01$, Figure 2c and d). The substitution of Er^{3+} by Zr^{4+} reduces the number of hole carriers³⁰ and alters the electronic domain wall transport and electrostatics.³¹ A quantitative analysis of the domain wall structure in both undoped and Zr-doped samples is presented in Figure 2e,f for trimerization angle Φ and amplitude Q . We find that the distributions of the trimerization angle Φ (averaged along the direction of the wall as described in SI Note 1) in Figure 2e reflects that both neutral and charged domain walls have a nonzero width, with neutral walls being slightly narrower than charged walls. All neutral walls observed in our sample are structurally equivalent, corresponding to so-called type A walls defined in ref 19 (see also refs 14, 15, and 20).

The distribution of atomic displacements across the domain wall in ErMnO_3 and $\text{Er}_{1-x}\text{Zr}_x\text{MnO}_3$ can be rationalized according to the Landau energy (eq 2) in terms of the corresponding material parameters. The solid lines in Figure 2e,f are obtained from the analytical solution of the minimization problem for the Landau energy, which reproduces the experimental data remarkably well. Specifically, the trimerization phase Φ is obtained from the Euler–Lagrange equation $\partial F/\partial \Phi = \vec{\nabla} \cdot \partial F/\partial (\nabla \Phi)$ under the approximation of low anisotropy of the Landau energy, that is, assuming that the amplitude keeps its bulk value Q_0 across the wall.^{32,33} Thus, the equation reduces to

$$\sin 6\Phi - \frac{\xi_6^2}{d^2} \frac{d^2(6\Phi)}{dx^2} = 0 \quad (3)$$

where x is the coordinate perpendicular to the wall. The nonlinear eq 3 is mathematically equivalent to the equation of motion of a pendulum, from which we obtain the evolution of Φ across a wall separating domains with $\Phi_n = n\pi/3$ and Φ_{n+1} as

$$\Phi(x) = \Phi_n + \frac{2}{3} \arctan(e^{x/\xi_6}) \quad (4)$$

The correction $\delta Q(x)$ to the constant-amplitude approximation [$Q(x) = Q_0 + \delta Q(x)$] due to the coupling with Φ is obtained by substituting eq 4 into the second Euler–Lagrange equation $\partial F/\partial Q = \vec{\nabla} \cdot \partial F/\partial (\nabla Q)$ and linearizing it with respect to $\delta Q(x)$. This yields

$$\delta Q(x) \approx -\frac{\xi_6^2}{\kappa \xi_6 \bar{\xi}_6} \frac{Q_0}{\cosh^2(x/\bar{\xi}_6)} \quad (5)$$

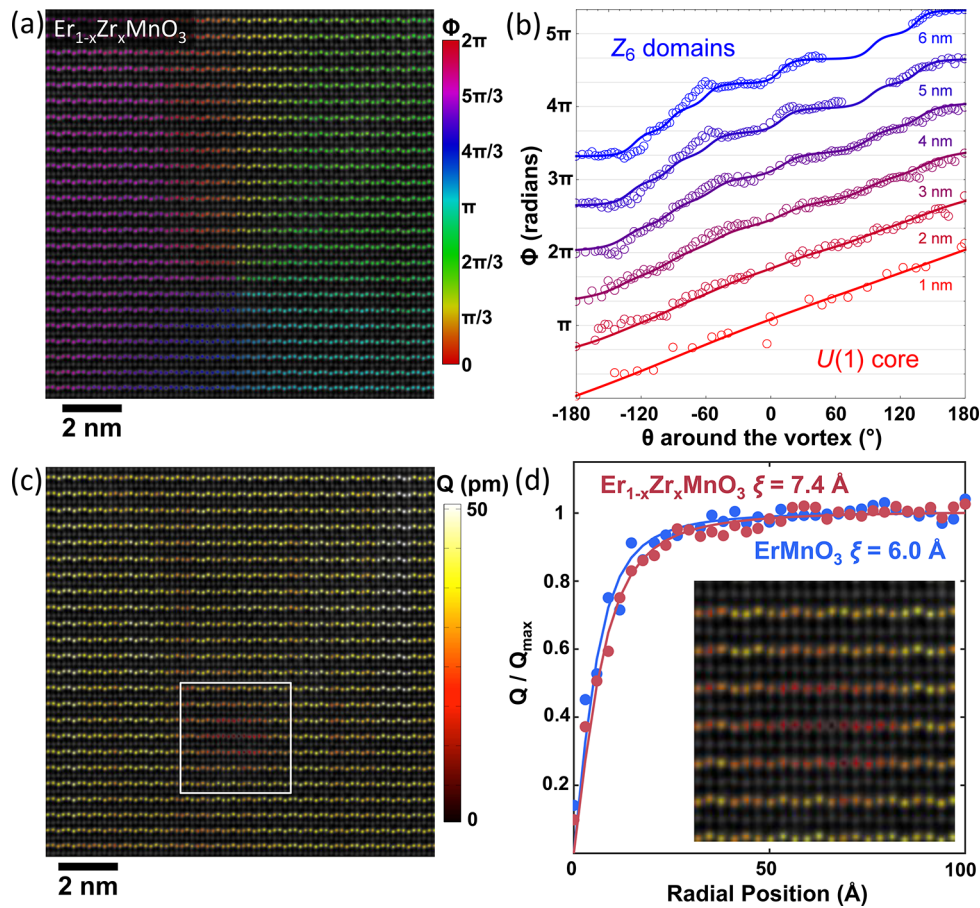


Figure 3. Atomic vortex structure. (a) HAADF-STEM overlay of the phase of the vortex in $\text{Er}_{1-x}\text{Zr}_x\text{MnO}_3$, showing a clockwise progression of phase from 0 to 2π . (b) The evolution of the phase wrapping around the vortex core at different radii in $\text{Er}_{1-x}\text{Zr}_x\text{MnO}_3$. Within 3 nm of the vortex, the phase progresses continuously, while farther from the vortex the phase levels off at one of the six distinct domains. Dots represent experimental measurements, and solid lines show phase-field simulated results in Figure 4a. (c) Same HAADF-STEM image as (a) with amplitude overlay, showing a decrease of Q at the vortex core. (d) Plot of the amplitude Q as a function of radial distance from the vortex core for both the doped and undoped specimens, showing the amplitude drop to nearly zero at the core and approach bulk values far from the core. Dots represent experimental measurement, and solid lines show the analytical expression $Q(r) = \frac{r/\xi}{\sqrt{2 + (r/\xi)^2}} Q_0$ with fitted $\xi = 7.4 \text{ \AA}$ for the Zr-doped specimen and $\xi = 6.0 \text{ \AA}$ for the undoped specimen. The full data for the ErMnO_3 specimen are in Figure S3.

where $\bar{\xi}_6 = \xi_6 \sqrt{1 + \xi^2/\xi_6^2}$ and κ is a constant resulting from the interplay between ξ and ξ_6 ($\kappa \approx 9/\sqrt{2\pi}$ for $\xi \sim \xi_6$ and $\kappa \approx 9/2$ for $\xi_6 \gg \xi$, see SI Note 4). In Figure 2f κ is a fitting parameter that effectively incorporates higher order corrections. The validity of this approximate solution (see Figure 2e and f and SI Note 3) reveals that the Z_6 anisotropy is moderate in our system.

This analysis also reveals that the fundamental domain wall width, as obtained from the trimerization phase Φ in Figure 2e, is defined by ξ_6 (rather than ξ). From the fitting to eq 4 we find $\xi_6^{\text{charged}} = 7.4 \pm 0.2 \text{ \AA}$ ($7.5 \pm 0.3 \text{ \AA}$) and $\xi_6^{\text{neutral}} = 6.3 \pm 0.1 \text{ \AA}$ ($5.9 \pm 0.1 \text{ \AA}$) for ErMnO_3 ($\text{Er}_{1-x}\text{Zr}_x\text{MnO}_3$). From fitting the trimerization amplitude Q in Figure 2f to eq 5, we find values of $\bar{\xi}_6^{\text{charged}} = 18 \pm 1 \text{ \AA}$ ($16 \pm 7 \text{ \AA}$) and $\bar{\xi}_6^{\text{neutral}} = 13 \pm 2 \text{ \AA}$ ($10 \pm 1 \text{ \AA}$) for ErMnO_3 ($\text{Er}_{1-x}\text{Zr}_x\text{MnO}_3$). Error bars represent the statistical uncertainty in the mean. An additional source of error originates from domains that overlap in the projection direction, leading to apparently wider domain walls as discussed in ref 17. To minimize such broadening effects, we use a thinner specimen ($\sim 20\text{--}50 \text{ nm}$) with a lower domain wall density and, hence, less overlap of domains. In fact, the contrast

of the atomic columns does not show evidence for domain overlap in our images (see Supplementary Figure S5 and SI Note 1). We also note that some misalignment of the domain walls with respect to the crystal lattice generally appears at large scales, as can be seen in Figure 2. In our statistical analysis of the walls, we averaged over more than 35 domain walls for each type of wall shown in Figure 2. To minimize additional sources of uncertainty (e.g., due to the meandering of the walls), we only considered areas in which the walls do not deviate more than 5 degrees from the vertical (or the horizontal) for the analysis in Figure 2e,f.

The obtained difference between ξ_6^{charged} and ξ_6^{neutral} can be understood as the result of the anisotropy in the gradient term ($\frac{\xi}{2} |\partial_i \mathbf{Q}|^2 \rightarrow \frac{\xi_x}{2} |\partial_i \mathbf{Q}|^2$ in eq 2, with $g_x = g_y \neq g_z$), as it is in tune with the difference that is obtained from DFT calculations of the corresponding parameters.²¹ Additional modifications may occur due to the chemical environment as indicated by the width of the neutral domain walls, which are about 6% thinner in $\text{Er}_{1-x}\text{Zr}_x\text{MnO}_3$ ($x = 0.01$) than in ErMnO_3 . It remains to be demonstrated, however, whether the observed change is due to the Zr doping or other growth-related parameters.

Furthermore, our analysis supports our experimental observation that the system displays low-symmetry regions with $\Phi \neq \frac{n\pi}{3}$ due to the gradual evolution of the trimerization across the domain walls. These regions explain the emergence of the continuous distribution of tilt angles Φ in Figure 1c that blurs the six discrete states expected according to the Z_6 symmetry of the bulk. The low-symmetry regions are expected to gain an increasingly dominant weight as the ferroelectric transition temperature is approached or if the 6-fold anisotropy is reduced, since they grow as $\xi_6 \sim |c'|^{-1/2} |T - T_c|^{-1}$. Interestingly, we note that the phase change across the trimerization domain walls is systematically slightly below its nominal value $\pm \pi/3$, which can be related to the residual symmetry breaking discussed in ref 29. To reproduce this feature in Figure 2e, we renormalize the solution (eq 4) to the corresponding experimental values in the bulk. The result is virtually indistinguishable from what can be obtained self-consistently using the Landau energy in ref 29.

Equation 4 is in fact the $k = 1$ case in the family of solutions to eq 3 that can be parametrized as $\Phi(x, k) = \frac{1}{6} \left[\pi + 2am \left(\frac{x}{k\xi_6} \middle| k^2 \right) \right]$ where $am(ulm)$ is the Jacobi amplitude function. In this family, the solutions with $k < 1$ describe the topological stripe domain states that occur when the system is grown below the trimerization transition temperature.³⁴ Accordingly, when $k \rightarrow 1^-$, these solutions lead to stripe domains of size $2k\xi_6 K(k)$ separated by domain walls of width ξ_6 (here, $K(k)$ is the complete elliptic integral of the first kind). Interestingly, if extended to the cylindrical geometry, this set of solutions can also describe the phase in trimerization vortices discussed below (see the SI Note 5 for details).

Vortex Structures. After clarifying the inner structure of the domain walls, we now turn to the topological defects that are observed in the form of a vortex-like distribution of the trimerization order parameter. This distribution is found wherever domain walls intersect, which systematically happens in groups of six.⁴ Figure 3 shows HAADF-STEM data of such a trimerization vortex in $\text{Er}_{1-x}\text{Zr}_x\text{MnO}_3$ (see SI Note 2 for ErMnO_3 data). Figure 3a shows the data for the trimerization phase, Φ , where in the HAADF-STEM image we can see six domains with different Φ_n 's merge at the central point of the vortex. The domain merging is analyzed in the Figure 3b, where we plot the trimerization phase Φ as a function of the angle θ around the central point of the vortex for different distances from this point (STEM data are marked by dots). Here, Φ exhibits step-like variations for distances $\gtrsim 3$ nm where it corresponds to a discrete set of trimerization domains separated by domain walls, in what we call the outer vortex region. In contrast, below ~ 3 nm, Φ becomes a continuous function and eventually displays a linear increase, $\Phi = \theta$, in the innermost part of the vortex (here and hereafter we use cylindrical (r, θ, z) coordinates). This analysis thus reveals that the center of the vortex is in fact a singular point in which $|\nabla\Phi(\theta)| \approx 1/r$ diverges. The data for the trimerization amplitude are shown in Figure 3c, for the same HAADF-STEM image. Figure 3d shows that the trimerization amplitude Q drops to zero at the vortex central point, recovering its bulk value within a distance of ≈ 22 Å for $\text{Er}_{1-x}\text{Zr}_x\text{MnO}_3$ (≈ 18 Å in ErMnO_3 —see SI Note 2 for additional data for undoped vortex). The bulk value of Q is near 28 pm (i.e., 42 pm of maximal relative displacement between Er atoms)—agreeing with previously reported values of Er displacements in the literature.¹⁹ These features can be

accurately reproduced by finite element modeling based on the minimization of the free energy in eq 2 as summarized in Figure 4 (see SI Note 6 for details on the finite element

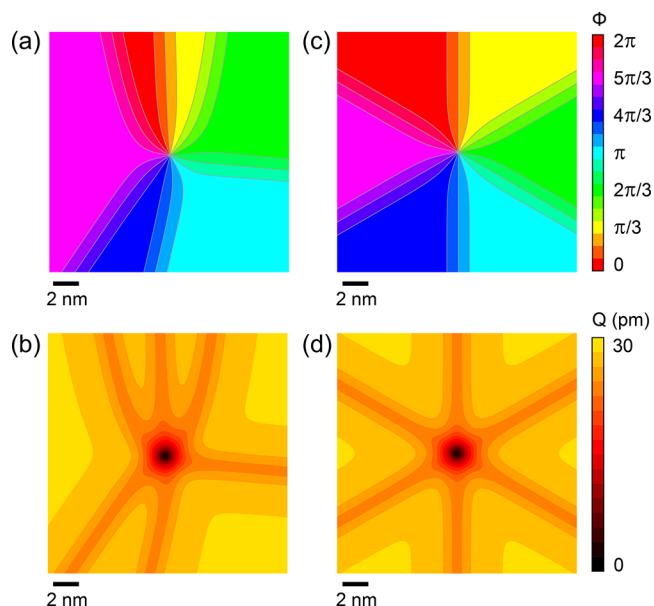


Figure 4. Contour plot for the local evolution of the trimerization order parameter at vortices. (a, b) Numerical simulations of the phase (a) and the amplitude (b) of a nonsymmetrical vortex, with the asymmetries present in Figure 3. (c, d) Same as a, b, for a symmetric vortex.

modeling). The coefficients of the Landau description are chosen to reproduce the correlation lengths ξ (see below) and ξ_6 obtained experimentally. Figure 4a,b presents the distribution of trimerization phase and amplitude in the vortex with a similar structure as the one in Figure 3a, and Figure 4c,d shows a symmetric vortex in which the six domains are equally represented. The calculated distribution of the phase from Figure 4a is also plotted in Figure 3b (solid lines), showing good agreement between theory and experiment.

The key features of the vortices can also be captured by a more phenomenological description based on the same analytical approach that reproduces the domain walls and topological stripes (see SI Note 5). One of the main conclusions of the analysis is that, in terms of the trimerization phase, the size of the vortex inner region is controlled by the characteristic length ξ_6 , that is, the same length that controls the size of the domain walls in the outer vortex region. In fact, the transition from the outer to the inner region can be seen as the result of domain walls overlapping as they approach the center of the vortex. Furthermore, the continuous winding of Φ in the inner vortex region (seen as the gradual increase of Φ in Figure 3b) is a striking manifestation of the fact that the trimerization cannot adapt to spatial variations below ξ_6 . Accordingly, we find that the curvature of the walls is also limited by this characteristic length ξ_6 .

Remarkably, the symmetry of the host lattice is irrelevant for the inner vortex region where the vortices become continuous with emergent $U(1)$ symmetry. As a result of this $Z_6 \rightarrow U(1)$ transformation, the central part of the trimerization vortex becomes completely analogous to a superfluid vortex. In fact, the interplay between Φ and Q is such that the minimization of the Landau energy (eq 2) in this inner $U(1)$ region gives that

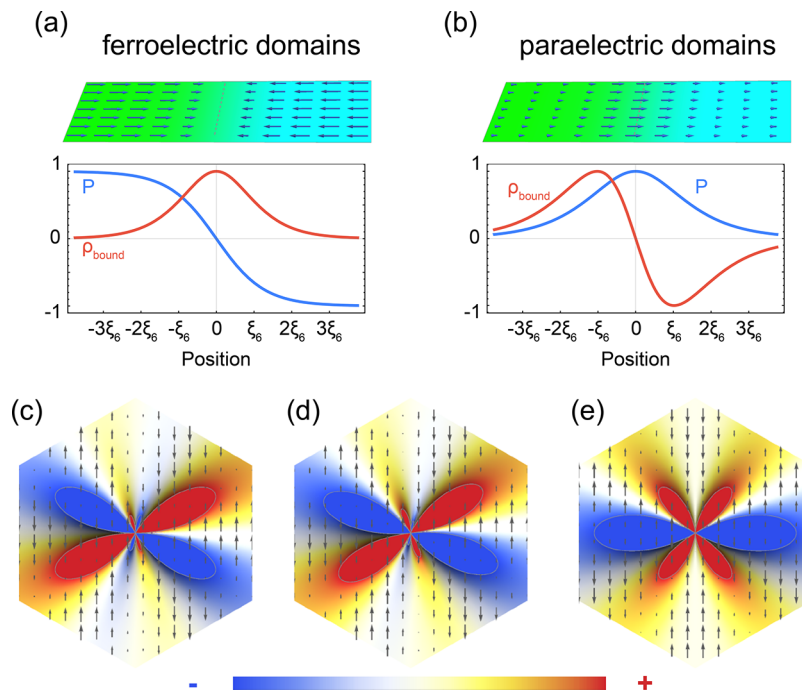


Figure 5. Emergent electrostatics at trimerization domain walls and vortices. (a,b) Trimerization domain wall separating ferroelectric (a) and nonferroelectric (b) domains. The arrows in the top panels represent the electric polarization resulting from the trimerization. In both cases, we observe the emergence of a nonzero distribution of bound charges localized at the wall due to the longitudinal variation of the polarization across the wall (bottom panels). (c–e) Density plot of the bound-charge distribution emerging at the core of the trimerization vortices (i.e., within a distance $\lesssim \xi_6$) for various orientations of the trimerization pattern with respect to the crystallographic axes Φ_0 (see eq 7), with superimposed arrows representing the electric polarization. The values of Φ_0 are 0 (c), $\pi/18$ (d), and $\pi/6$ (e). In general, we observe eight bound-charge lobes of different size due to the gradual modulation of polarization within the core (c,d). The relative orientation of the trimerization pattern determines the size of the lobes, some of which can become vanishingly small as in panel e.

the trimerization amplitude is $Q(r) \approx \frac{r/\xi}{\sqrt{2+(r/\xi)^2}} Q_0$. As a consequence, the vortex develops a “hard” core of the size $\sim \xi$ where the trimerization amplitude drops linearly to zero. This behavior is reproduced in Figure 3d, where we show this distribution of the trimerization amplitude (solid line) along with $Q(r)$ extracted from TEM (dots).

As we see, the stiffnesses associated with ξ_6 and ξ ultimately generate a transition between several distinct regions of the trimerization vortices: from the outermost Z_6 part that displays well-defined domains ($\Phi_n = \frac{n\pi}{3}$, $Q = \text{const}$), to the inner vortex regions where the discrete nature of Φ is lost [$U(1)$ symmetry, $\Phi \approx \theta$, size $\sim \xi_6$] and Q drops to zero [$Q(r) \approx \frac{r/\xi}{\sqrt{2+(r/\xi)^2}} Q_0$, size $\sim \xi$]. We note that ξ_6 and ξ are two independent scales of the system that can easily be of different orders of magnitude, especially near the trimerization transition where $\xi_6/\xi = \sqrt{b^2/(3la(T)||c'})} \rightarrow \infty$ as $T \rightarrow T_c$ or by means of the appropriate doping (such that $|c'| \rightarrow 0$). In that case, the vortex inner regions will dominate the response of the system and enforce an emergent $U(1)$ behavior of the order parameter with Q close to its bulk value. Thus, we are identifying ξ_6 as the principal characteristic length defining the morphology of topological defects in h-RMnO₃.

Emergent Electrostatics at Domain Walls and Vortices. Our data gained on ErMnO₃ and Er_{1-x}Zr_xMnO₃ demonstrate that the global structure of the topological defects observed in these systems is primarily determined by the trimerization order parameter, with their electric-charge properties playing only a minor role. The local electrostatics

is a source of diverse functional behavior, potentially codetermining the interaction between topological defects and the interplay with other charged defects, such as oxygen vacancies, interstitials, and dopants. Furthermore, we expect the local charges that emerge at the topological defects to extend to distances $\sim \xi_6$, that is, a distance which is largely independent of the surrounding electrostatics. Hence, the local charges are expected to be distributed over divergingly large areas near the transition point and/or in systems with reduced anisotropy. In this case the topological defects will all display the same emergent symmetries associated with their inner structure, leading to a generalized electrostatics that will draw apart from the surrounding bulk.

Figure 5a,b shows calculations comparing the charge distribution and the polarization across the domain walls directed perpendicularly to the c -direction in two types of material—in a ferroelectric ($c' < 0$) and in a paraelectric ($c' > 0$) RMnO₃. Figure 5a corresponds to a positively charged ferroelectric head-to-head wall similar to that seen in Figure 2c. The calculations show that the charge of the domain wall is distributed over the distance $\sim \xi_6$, corresponding to the variation in the polarization and, hence, the variation of the trimerization phase. A qualitatively different type of wall is shown in Figure 5b. The latter exemplifies a domain wall separating nonferroelectric domains as can be realized under certain conditions in hexagonal InMnO₃.^{35,36} In this case, there is a nonzero electric polarization induced at the domain wall due to the continuous change of the trimerization phase across the wall. Despite $\nabla \cdot \mathbf{P} \neq 0$ inside the wall, the charge integrated over it is zero, and so the wall is neutral in the sense that no

long-range electric fields are generated by the bound charges. However, the distribution of charge provides a dipolar character due to the localization of the polarization—in fact, the wall represents a ferroelectric 2D system with tunable size ξ_6 .

Despite the strikingly different nature of the domain walls in Figure 5a,b, we note that their meeting points (i.e., the vortices) exhibit the same features due to the emerging U(1) symmetry. Most remarkably, the inner vortex region displays rather unexpected electrostatics irrespective of the ferroelectric or nonferroelectric character of the corresponding domains (Figure 5c–e). Specifically, the trimerization at the center of the vortices becomes sinusoidally modulated and generates a gradual distribution of polarization

$$\mathbf{P} \propto \frac{(r/\xi)^3}{[2 + (r/\xi)^2]^{3/2}} \cos(3(\Phi - \Phi_0)) Q_0^3 \hat{\mathbf{z}} \quad (6)$$

Equation 6 applies for vortices lying in the xz - or yz -plane, where Φ_0 denotes the trimerization origin with respect to the z -axis. As such, it is a universal distribution that leads to an intriguing pattern of bound charges in which both radial and angular variations of the polarization play a role. The charge distribution is

$$\rho_{\text{bound}} = \nabla \cdot \mathbf{P} = \frac{-3(r/\xi)^2}{2[2 + (r/\xi)^2]^{5/2}} \left[(r/\xi)^2 \sin(4\Phi - 3\Phi_0) + \left[4 + \left(\frac{r}{\xi}\right)^2 \right] \sin(2\Phi - 3\Phi_0) \right] \rho_0 \quad (7)$$

Equations 6 and 7 can be traced back to the emergent U(1) symmetry and reveal that, as the central point of the vortex is approached, bound charges delocalize from the nominal positions of the walls to form a more complex pattern. Outside the hard-core of the vortex ($\xi < r < \xi_6$) an octupolar-like charge pattern occurs as illustrated in Figure 5c–e. In contrast, the distribution transforms into a quadrupolar-like one in the hard-core region ($r < \xi$), in which, however, the charge is strongly suppressed due to the vanishing of the trimerization amplitude near the $\nabla\Phi$ singularity.

Similar to the trimerization domain walls, the vortex bound charges require screening by mobile charge carriers and are thus anticipated to lead to anomalous electronic transport behavior. Since the size of the vortex inner region can be rather small far from T_C , the related transport phenomena can be hidden from established probe techniques such as conductive atomic force microscopy (cAFM). Our theory shows, however, that the vortex inner regions grow with ξ_6 . In consequence we anticipate that, irrespective of whether or not bulk ferroelectricity appears below the transition, the anomalous vortex transport can be detectable if the structural transition is driven to an experimentally accessible interval (e.g., by means of finite-size effects in thin films or epitaxial strain³⁷). Alternatively, vortex transport may be obtained by doping to engineer the effective anisotropy of the system.

Conclusions. Hexagonal manganites develop a rich variety of topological defects, including neutral, positively, and negatively charged domain walls, as well as special vortices. Our work explains the atomic structure of these topological objects by combining state-of-the-art scanning transmission electron microscopy and the universal framework of the Landau theory of phase transitions. Independent of their specific 2D or 1D nature, they exhibit an inner structure that is fundamentally

determined by a single critical length scale (ξ_6). This length scale relates to the structural stiffness of the system rather than to its charge properties. As a consequence, domain walls with diverging electrostatic potentials and neutral domain walls have a similar structural width, representing a striking example for the unique consequences of improper ferroelectricity at the atomic scale. Furthermore, completely new and so far unexplored electrostatics arise at the vortices where improper ferroelectric domain walls intersect. Here, the hexagonal bulk structure becomes irrelevant, leading to octupolar- and quadrupole-like electrostatic field configurations. Similar to the charged domain walls, vortices thus represent a promising source for unusual electronic transport properties at the nanoscale.

■ ASSOCIATED CONTENT

Supporting Information

The Supporting Information is available free of charge on the ACS Publications website at DOI: 10.1021/acs.nanolett.7b01288.

Note 1, STEM data acquisition and processing; Note 2, STEM observations of vortex in undoped ErMnO₃; Note 3, justification of the constant-amplitude approximation for eq 4; Note 4, analytical description of trimerization amplitude at the wall; Note 5, analytical description of trimerization order parameter in the vortex; Note 6, numerical description of trimerization order parameter in the vortex (PDF)

■ AUTHOR INFORMATION

Corresponding Authors

*E-mail: dennis.meier@ntnu.no.

*E-mail: andres.cano@cnrs.fr.

ORCID

Konstantin Shapovalov: 0000-0002-7978-2986

Author Contributions

M.E.H. and K.S. contributed equally to this work. A.C. and D.M. initiated and coordinated the project. M.E.H., J.A.M., and C.S.C. conducted the STEM experiments, and M.E.H. analyzed the data, with supervision from D.A.M. K.S. and A.C. provided the analytical description, and K.S. conducted the numerical calculations. E.B. and Z.Y. grew the single crystals. All authors participated in the discussion and interpretation of the results. A.C., D.M., M.E.H., and K.S. cowrote manuscript.

Funding

Electron microscopy work was supported by the U.S. Department of Energy, Office of Basic Energy Sciences, Division of Materials Sciences and Engineering under award no. DE-SC0002334. This work made use of the electron microscopy facility of the Cornell Center for Materials Research Shared Facilities which are supported through the NSF MRSEC program (DMR-1120296). D.M. acknowledges funding from NTNU and Onsager Fellowship Programme. E.B. and Z.Y. were supported in part by the US Department of Energy and carried out at the Lawrence Berkeley National Laboratory under contract no. DE-AC02-05CH11231. A.C. and K.S. were supported by the French Government “Investments for the Future” Program, University of Bordeaux Initiative of Excellence (IDEX Bordeaux).

Notes

The authors declare no competing financial interest.

ACKNOWLEDGMENTS

We would like to thank Mick Thomas, John Grazul, and Dr. Earl Kirkland for assistance in the microscope facilities. We thank S. M. Selbach, D. R. Småbråten, and E. Padgett for discussions.

REFERENCES

- (1) The Nobel Prize in Physics 2016 - Advanced Information. Nobelprize.org. Nobel Media AB 2014. http://www.nobelprize.org/nobel_prizes/physics/laureates/2016/advanced.html (accessed Sep 13, 2017).
- (2) Mermin, N. D. *Rev. Mod. Phys.* **1979**, *51*, 591–649.
- (3) Meier, D. *J. Phys.: Condens. Matter* **2015**, *27*, 463003.
- (4) Choi, T.; Horibe, Y.; Yi, H. T.; Choi, Y. J.; Wu, W.; Cheong, S.-W. *Nat. Mater.* **2010**, *9*, 253–258.
- (5) Seidel, J.; Vasudevan, R. K.; Valanoor, N. *Adv. Electron. Mater.* **2016**, *2*, 1500292.
- (6) Wiesendanger, R. *Nat. Rev. Mater.* **2016**, *1*, 16044.
- (7) Seidel, J. *Topological structures in ferroic materials*; Springer International Publishing, 2016.
- (8) Fert, A.; Cros, V.; Sampaio, J. *Nat. Nanotechnol.* **2013**, *8*, 152–156.
- (9) Griffin, S. M.; Lilienblum, M.; Delaney, K. T.; Kumagai, Y.; Fiebig, M.; Spaldin, N. A. *Phys. Rev. X* **2012**, *2*, 041022.
- (10) Lin, S.-Z.; Wang, X.; Kamiya, Y.; Chern, G.-W.; Fan, F.; Fan, D.; Casas, B.; Liu, Y.; Kiryukhin, V.; Zurek, W. H.; et al. *Nat. Phys.* **2014**, *10*, 970–977.
- (11) Meier, Q. N.; Lilienblum, M.; Griffin, S. M.; Conder, K.; Pomjakushina, E.; Yan, Z.; Bourret, E.; Meier, D.; Lichtenberg, F.; Salje, E. K. H., et al. *arXiv:1703.08321*, **2017**.
- (12) Meier, D.; Seidel, J.; Cano, A.; Delaney, K.; Kumagai, Y.; Mostovoy, M.; Spaldin, N. A.; Ramesh, R.; Fiebig, M. *Nat. Mater.* **2012**, *11*, 284–288.
- (13) Geng, Y.; Das, H.; Wysocki, A. L.; Wang, X.; Cheong, S.-W.; Mostovoy, M.; Fennie, C. J.; Wu, W. *Nat. Mater.* **2013**, *13*, 163–167.
- (14) Zhang, Q. H.; Wang, L. J.; Wei, X. K.; Yu, R. C.; Gu, L.; Hirata, A.; Chen, M. W.; Jin, C. Q.; Yao, Y.; Wang, Y. G.; et al. *Phys. Rev. B: Condens. Matter Mater. Phys.* **2012**, *85*, 020102.
- (15) Matsumoto, T.; Ishikawa, R.; Tohei, T.; Kimura, H.; Yao, Q.; Zhao, H.; Wang, X.; Chen, D.; Cheng, Z.; Shibata, N.; et al. *Nano Lett.* **2013**, *13*, 4594–4601.
- (16) Zhang, Q.; Tan, G.; Gu, L.; Yao, Y.; Jin, C.; Wang, Y.; Duan, X.; Yu, R. *Sci. Rep.* **2013**, *3*, 2741.
- (17) Li, J.; Chiang, F.-K.; Chen, Z.; Ma, C.; Chu, M.-W.; Chen, C.-H.; Tian, H.; Yang, H.; Li, J. *Sci. Rep.* **2016**, *6*, 28047.
- (18) Huang, F.-T.; Cheong, S.-W. *Nat. Rev. Mater.* **2017**, *2*, 17004.
- (19) Han, M.-G.; Zhu, Y.; Wu, L.; Aoki, T.; Volkov, V.; Wang, X.; Chae, S. C.; Oh, Y. S.; Cheong, S.-W. *Adv. Mater.* **2013**, *25*, 2415–2421.
- (20) Huang, F.-T.; Wang, X.; Griffin, S. M.; Kumagai, Y.; Gindele, O.; Chu, M.-W.; Horibe, Y.; Spaldin, N. A.; Cheong, S.-W. *Phys. Rev. Lett.* **2014**, *113*, 267602.
- (21) Artyukhin, S.; Delaney, K. T.; Spaldin, N. A.; Mostovoy, M. *Nat. Mater.* **2013**, *13*, 42–49.
- (22) Kumagai, Y.; Spaldin, N. A. *Nat. Commun.* **2013**, *4*, 1540.
- (23) Fennie, C. J.; Rabe, K. M. *Phys. Rev. B: Condens. Matter Mater. Phys.* **2005**, *72*, 100103.
- (24) Van Aken, B. B.; Palstra, T. T. M.; Filippetti, A.; Spaldin, N. A. *Nat. Mater.* **2004**, *3*, 164–170.
- (25) Lilienblum, M.; Lottermoser, T.; Manz, S.; Selbach, S. M.; Cano, A.; Fiebig, M. *Nat. Phys.* **2015**, *11*, 1070–1073.
- (26) Chae, S. C.; Lee, N.; Horibe, Y.; Tanimura, M.; Mori, S.; Gao, B.; Carr, S.; Cheong, S.-W. *Phys. Rev. Lett.* **2012**, *108*, 167603.
- (27) Das, H.; Wysocki, A. L.; Geng, Y.; Wu, W.; Fennie, C. J. *Nat. Commun.* **2014**, *5*, 2998.
- (28) Mundy, J. A.; Brooks, C. M.; Holtz, M. E.; Moyer, J. A.; Das, H.; Rébola, A. F.; Heron, J. T.; Clarkson, J. D.; Disseler, S. M.; Liu, Z.; et al. *Nature* **2016**, *537*, 523–527.
- (29) Cano, A. *Phys. Rev. B: Condens. Matter Mater. Phys.* **2014**, *89*, 214107.
- (30) Van Aken, B. B.; Bos, J.-W. G.; de Groot, R. A.; Palstra, T. T. M. *Phys. Rev. B: Condens. Matter Mater. Phys.* **2001**, *63*, 125127.
- (31) Schaab, J.; Cano, A.; Lilienblum, M.; Yan, Z.; Bourret, E.; Ramesh, R.; Fiebig, M.; Meier, D. *Adv. Electron. Mater.* **2016**, *2*, 1500195.
- (32) Tagantsev, A.; Cross, L. E.; Fousek, J. *Domains in Ferroic Crystals and Thin Films*; Springer International Publishing, 2010.
- (33) Strukov, B. A.; Levanyuk, A. P. *Ferroelectric Phenomena in Crystals*; Springer International Publishing, 1998.
- (34) Chae, S. C.; Horibe, Y.; Jeong, D. Y.; Rodan, S.; Lee, N.; Cheong, S.-W. *Proc. Natl. Acad. Sci. U. S. A.* **2010**, *107*, 21366–21370.
- (35) Kumagai, Y.; Belik, A. A.; Lilienblum, M.; Leo, N.; Fiebig, M.; Spaldin, N. A. *Phys. Rev. B: Condens. Matter Mater. Phys.* **2012**, *85*, 174422.
- (36) Huang, F. T.; Wang, X.; Oh, Y. S.; Kurushima, K.; Mori, S.; Horibe, Y.; Cheong, S.-W. *Phys. Rev. B: Condens. Matter Mater. Phys.* **2013**, *87*, 184109.
- (37) Pang, H.; Zhang, F.; Zeng, M.; Gao, X.; Qin, M.; Lu, X.; Gao, J.; Dai, J.; Li, Q. *npj Quantum Materials* **2016**, *1*, 16015.